Submission for The Journal of the Acoustical Society of America
March 3, 2005

Iterative simulation of elastic wave scattering in arbitrary dispersions of spherical particles

Timothy E. Doyle
Department of Physics
Utah State University, Logan, Utah 84322

A numerical modeling approach was developed to simulate the propagation of shear and longitudinal sound waves in arbitrary, dense dispersions of spherical particles. The scattering interactions were modeled with vector multipole functions and boundary condition solutions for each particle. Multiple scattering was simulated by translating the scattered wave fields from one particle to another with the use of translational addition theorems, summing the multiple-scattering contributions, and recalculating the scattering using an iterative method. The theory and initial results for the model are presented, including an integral derivation for the translational addition theorems. The model can simulate 3D material microstructures with a variety of particle size distributions, compositions, and volume fractions. To test the model, spectra and wave field patterns were generated from both ordered and disordered microstructures containing up to several hundred particles. The model predicts wave propagation phenomena such as refractive focusing, mode conversion, and band gap phenomena. The convergence of the iterations ranges from excellent to fair, and is dependent on the field (longitudinal or shear), particle configuration, and elastic wave frequency. The model is currently limited by the computation of sufficiently high multipole order for the simulation of dense particle dispersions.

PACS numbers: 43.20.Gp, 43.35.Cg

I. INTRODUCTION

The propagation of elastic waves through particles randomly dispersed in a liquid or solid is relevant to many applications, including the nondestructive evaluation of particulate composites, the design of advanced acoustic materials, the process monitoring of suspensions, the ultrasonic examination of living tissues, and seismic models for various geologic media (sediments, rocks, etc.). Modeling elastic waves in such systems is difficult, however, due to multiple scattering between particles, mode conversion from scattering at particle surfaces, lack of periodicity in the particle configuration, and heterogeneity of particle sizes and compositions. Non-empirical, physics-based models are therefore desired to simulate elastic wave propagation in dense, random dispersions of particles and predict the resultant macroscopic wave propagation properties.

This paper presents the theory and results of a numerical model developed to address these goals. The model uses vector multipole functions, boundary condition solutions,

Report Documentation Page

Form Approved
OMB No. 0704-0188

1. REPORT DATE	2. REPORT TYPE	3. DATES COVERED
MAR 2005		**-**

4. TITLE AND SUBTITLE
Iterative Simulation of Elastic Wave Scattering in Arbitrary Dispersions of Spherical Particles

5a. CONTRACT NUMBER

5b. GRANT NUMBER

5c. PROGRAM ELEMENT NUMBER

6. AUTHOR(S)
Timothy Doyle

5d. PROJECT NUMBER
1011

5e. TASK NUMBER
00NF

5f. WORK UNIT NUMBER

7. PERFORMING ORGANIZATION NAME(S) AND ADDRESS(ES)
ATK Thiokol, Inc.,P.O. Box 707, M/S 200,Brigham City,UT,84302-0707

8. PERFORMING ORGANIZATION REPORT NUMBER

9. SPONSORING/MONITORING AGENCY NAME(S) AND ADDRESS(ES)

10. SPONSOR/MONITOR'S ACRONYM(S)

11. SPONSOR/MONITOR'S REPORT NUMBER(S)

12. DISTRIBUTION/AVAILABILITY STATEMENT
Approved for public release; distribution unlimited

13. SUPPLEMENTARY NOTES

14. ABSTRACT

A numerical modeling approach was developed to simulate the propagation of shear and longitudinal sound waves in arbitrary, dense dispersions of spherical particles. The scattering interactions were modeled with vector multipole functions and boundary condition solutions for each particle. Multiple scattering was simulated by translating the scattered wave fields from one particle to another with the use of translational addition theorems, summing the multiple-scattering contributions, and recalculating the scattering using an iterative method. The theory and initial results for the model are presented, including an integral derivation for the translational addition theorems. The model can simulate 3D material microstructures with a variety of particle size distributions, compositions and volume fractions. To test the model, spectra and wave field patterns were generated from both ordered and disordered microstructures containing up to several hundred particles. The model predicts wave propagation phenomena such as refractive focusing, mode conversion, and band gap phenomena. The convergence of the iterations ranges from excellent to fair, and is dependent on the field (longitudinal or shear), particle configuration, and elastic wave frequency. The model is currently limited by the computation of sufficiently high multipole order for the simulation of dense particle dispersions.

15. SUBJECT TERMS

16. SECURITY CLASSIFICATION OF:			17. LIMITATION OF ABSTRACT	18. NUMBER OF PAGES	19a. NAME OF RESPONSIBLE PERSON
a. REPORT	b. ABSTRACT	c. THIS PAGE			
unclassified	**unclassified**	**unclassified**		**29**	

translational addition theorems, and direct iteration to solve the multiple-scattering problem for an arbitrary distribution of spheres in a solid matrix. The model can calculate either the spatial patterns or frequency spectra of elastic wave fields for a simulated random particle configuration. Macroscopic properties such as attenuation and velocity can therefore be predicted for a wide variety of particulate systems.

Multiple scattering in particulate systems is not solvable in an exact, closed analytical form for an arbitrary number and arrangement of particles. Scattering models must therefore use either statistical formulations or numerical simulation. The simulation of elastic waves in complex particle dispersions is computationally exhausting, however, for many modeling approaches. Finite methods are the most widely used numerical approaches for modeling fields in physical systems, but are often limited to 2D representations or the use of periodic cells for the simulation of particle dispersions.[1-3] These simplifications reduce the number of calculations, but may also exclude effects arising from a fully random and 3D particle configuration.

Multipole approaches can be more efficient than finite methods for modeling systems with spherical, spheroidal, or cylindrical particles since a multipole field contains significantly more information than a field value at a grid point. Several multipole techniques have been developed for multiple scattering, including transfer matrix (T matrix) methods, fast multipole methods, and direct iterative methods (as opposed to iterative solution methods for matrix approaches).

The direct iterative method has been applied to electromagnetic scattering in small collections of spherical particles, where it is also known as the order-of-scattering method.[4-6] Direct iterative methods have yet to be applied, however, to fully random 3D particle systems with large numbers of particles (>100 particles), high particle concentrations (>20%), and mixed particle sizes and properties. Additionally, multipole-based acoustic models for particulate systems have been limited to either longitudinal wave propagation or periodic lattices of particles.[7-9] Little work has been reported on the modeling of full elastic wave scattering in random particulate systems, with longitudinal and shear waves in both particles and matrix.

There are a number of reasons to justify the use of a direct iterative approach over a T matrix, fast multipole, or unit-cell approach. The T matrix approach solves the multiple-scattering problem as a linear system of equations. In contrast, the direct iterative approach solves for multiple scattering by iteratively recomputing the multiple-scattering contributions until convergence of the elastic wave fields. Direct iterative methods are therefore computationally simpler and avoid the pitfalls of numerically inverting large matrices for large numbers of particles. Often, such matrices are solved using iterative methods, which could be argued as placing the direct iterative approach on the same level as the T matrix approach. However, the direct iterative approach sidesteps the need to explicitly formulate and solve the multiple scattering as a problem in linear algebra.

An additional advantage of the iterative approach is its correspondence to the physically intuitive order-of-scattering concept, where each iteration step represents a successive order of scattering. For example, the initial fields before iteration correspond to the zero-order contributions to multiple scattering (single-scattering approximation), the first iteration corresponds to the first-order contributions, the second iteration corresponds to the second-order

contributions, and so on. The ability to separately compute and inspect each successive scattering order provides a deeper understanding of the scattering process and of the effects of multiple scattering. It also provides a useful diagnostic of the model's performance and accuracy, and allows certain interactions to be excluded for computational efficiency (e.g., interactions between distant particles).

In comparison to fast multipole methods, the iterative approach treats the particle configurations in a more straightforward manner without resorting to segregation of the particles into groups with short-range (particle-to-particle) and long-range (group-to-group) interactions. The fast multipole method reduces the computations associated with such simulations by imposing a hierarchical scattering process that assumes material homogeneity at a sufficiently large scale above the particle level.[10] This assumption limits the applicability of the approach to macroscopically homogeneous composites with little spatial variation in the microstructure. The iterative multipole method, however, imposes no such restrictions on the material microstructure, and is additionally numerically simpler.

For ordered particle systems, unit cell methods employ periodic boundary conditions to model an infinite lattice, and this method has also been applied to random ensembles. The limitations of this method include the difficulty of modeling finite lattices ($<10^3$ particles), defects, and various levels of disorder. The unit cell approach may therefore be insufficient for modeling acoustic band gap phenomena for point and line defects, lattice heterostructures, and small acoustic band gap (phononic) crystals. When applied to random configurations (i.e., the unit cell is comprised of a random particle arrangement), the method introduces long-range order that may bias the model's results.

This paper presents the theory and initial results for an iterative multipole model developed for elastic wave propagation in particulate systems. The particles are modeled as spheres embedded in a solid matrix, permitting the use of spherical wave functions for the elastic wave fields. The model computes the propagation of waves by using single particle scattering solutions, addition theorems to translate the scattered fields from one particle to another, and iteration to compute the scattering resulting from the multiply scattered fields. Simulations were performed on a personal computer for particle systems of up to several hundred particles and particle volume fractions up to 50%. Initial results are presented for example simulations, and the capabilities and deficiencies of the current model are summarized. Methods for improving both the accuracy and efficiency of the model are discussed.

II. THEORY

A. Vector multipole functions

Spherical wave expansions form the theoretical basis for the iterative multipole method, and describe elastic waves derived from the Navier equation for linear, homogeneous materials:

$$\rho \frac{\partial^2 \mathbf{u}}{\partial t^2} = (\lambda + 2\mu)\nabla(\nabla \cdot \mathbf{u}) - \mu \nabla \times (\nabla \times \mathbf{u}) . \qquad (1)$$

Eq. (1) can be recast as two separate vector Helmholtz equations by splitting the displacement vector **u** into longitudinal and transverse parts and imposing an harmonic time dependency of the form $e^{-i\omega t}$:

$$(\nabla^2 + k_L^2)\mathbf{u}_L = 0, \tag{2}$$

$$(\nabla^2 + k_S^2)\mathbf{u}_S = 0. \tag{3}$$

Solutions to the vector Helmholtz equation in spherical coordinates are the vector spherical wave functions. The vector spherical wave functions in this work were constructed from spherical radial functions and vector spherical harmonics denoted as $z_n(kr)$ and $\mathbf{Y}_{nm}^{l}(\theta,\varphi)$ respectively. These functions are also referred to as vector multipole functions. The spherical radial functions are comprised of the spherical Bessel functions $j_n(kr)$ for standing waves inside the particles, spherical Hankel functions of the first kind $h_n^{(1)}(kr)$ for outward-propagating scattered waves, and spherical Hankel functions of the second kind $h_n^{(2)}(kr)$ for inward-propagating incident waves.

The vector spherical harmonics used in this work are eigenfunctions of the quantum angular momentum operators $\hat{\mathbf{J}}^2$, $\hat{J}_z$, $\hat{\mathbf{L}}^2$, and $\hat{\mathbf{S}}^2$, and are also known as pure-orbital vector spherical harmonics.[11-13] Using helicity basis vectors and scalar spherical harmonics they can be defined as

$$\begin{aligned}\mathbf{Y}_{nm}^{l}(\theta,\varphi) = {} & C_{l,m+1,1,-1}^{n,m} Y_{l,m+1}\mathbf{e}_{-1} \\ & + C_{l,m,1,0}^{n,m} Y_{l,m}\mathbf{e}_{0} + C_{l,m-1,1,1}^{n,m} Y_{l,m-1}\mathbf{e}_{+1}\end{aligned} \tag{4}$$

The *C*-symbols are the Clebsch-Gordan coefficients commonly used in quantum mechanics and derived from integrals involving three spherical harmonics. The notation used is from Varshalovich et al.[13] Vector functions are necessary for representing shear elastic fields, and the vector spherical harmonics provide a compact notation for otherwise awkward combinations of scalar spherical harmonics.

Since they are solutions to the Helmholtz equation, the vector multipole functions can be generated from a scalar potential Φ and vector potential $\boldsymbol{\Psi}$ defined as following:

$$\Phi = \sum_{n=0}^{\infty}\sum_{m=-n}^{+n} z_n(kr)Y_{nm}(\theta,\varphi) \tag{5}$$

$$\boldsymbol{\Psi} = \sum_{n=0}^{\infty}\sum_{m=-n}^{+n} z_n(kr)\mathbf{Y}_{nm}^{n}(\theta,\varphi) \tag{6}$$

The vector multipole functions are derived by applying the gradient and curl operations to the potentials in the following manner:

$$\mathbf{U} = \frac{1}{k}\nabla\Phi \tag{7}$$

$$\mathbf{V} = \frac{1}{k}\nabla\times\boldsymbol{\Psi} \tag{8}$$

$$\mathbf{W} = \frac{1}{k^2}\nabla\times\left(\nabla\times\boldsymbol{\Psi}\right) \tag{9}$$

The resulting vector multipole functions are complete and orthogonal multipole expansions for $n = 0$ to ∞ and $m = -n$ to $+n$, and are the following:

$$\mathbf{U} = \sum_{n=0}^{\infty}\sum_{m=-n}^{+n}\left(\sqrt{\frac{n}{2n+1}}z_{n-1}(kr)\mathbf{Y}_{nm}^{n-1}(\theta,\varphi) + \sqrt{\frac{n+1}{2n+1}}z_{n+1}(kr)\mathbf{Y}_{nm}^{n+1}(\theta,\varphi)\right) \tag{10}$$

$$\mathbf{V} = \sum_{n=0}^{\infty}\sum_{m=-n}^{+n}\left(i\sqrt{\frac{n+1}{2n+1}}z_{n-1}(kr)\mathbf{Y}_{nm}^{n-1}(\theta,\varphi) - i\sqrt{\frac{n}{2n+1}}z_{n+1}(kr)\mathbf{Y}_{nm}^{n+1}(\theta,\varphi)\right) \tag{11}$$

$$\mathbf{W} = \sum_{n=0}^{\infty}\sum_{m=-n}^{+n}z_n(kr)\mathbf{Y}_{nm}^{n}(\theta,\varphi) \tag{12}$$

U, **V**, and **W** are the longitudinal, electric, and magnetic vector multipole functions, respectively. They are similar to other widely used wave function and multipole formulations, specifically the **L**, **N**, and **M** vector spherical wave functions of Stratton[14]; the **A**(*r;L*), **A**(*r;E*), and **A**(*r;M*) vector multipoles of Greiner and Maruhn, Rose, and Edmonds[11,15,16]; and the **X** vector spherical harmonic of Jackson.[17] The **U**, **V**, and **W** functions, however, are specifically consistent with the definitions in Eqs. (5-9) as opposed to other vector multipole definitions, and provide a more compact notation than Stratton's vector spherical wave functions.

U corresponds to the longitudinal displacement field. **V** and **W** are transverse fields that can correspond to either elastic shear fields or electromagnetic fields. For elastic waves, **V** corresponds to the shear-electric displacement field (shear field with electric-type vector multipole function), and **W** corresponds to the shear-magnetic displacement field (shear field with magnetic-type vector multipole function). The horizontal and vertical conventions normally used to differentiate the two types of shear fields are not used here due to the ambiguity of distinguishing vertical and horizontal orientations in a spherical coordinate system.

The initial waves incident on the particles are modeled as plane waves. The spherical expansion for the longitudinal plane wave is derived from the gradient of the partial wave expansion for scalar fields:

$$\begin{aligned}\mathbf{e}_z e^{ikz} &= \frac{1}{ik}\nabla e^{ikz} \\ &= \frac{1}{ik}\nabla\left[\sum_{n=0}^{\infty} i^n \sqrt{4\pi(2n+1)}\, j_n(kr) Y_{n,0}(\theta,\varphi)\right]. \\ &= \sum_{n=0}^{\infty} i^{n-1}\sqrt{4\pi(2n+1)}\mathbf{U}_{n,0}\end{aligned} \tag{13}$$

At least three different partial wave expansions have been presented in the literature for transverse vector planes waves, including those by Stratton,[14] Jackson,[17] and Greiner and Maruhn.[11] Extensive mathematical analysis and numerical testing, however, has shown that the expansions of Greiner and Maruhn present the correct formulation and consistently converge. These expansions were reformulated for the **U**, **V**, and **W** functions, and for shear waves propagating in the *z* direction and polarized in the *x* and *y* directions. These partial wave expansions are the following:

$$\mathbf{e}_x e^{ikz} = \sum_n i^n \sqrt{\pi(2n+1)}\left[\mathbf{W}_{n,+1} + \mathbf{V}_{n,+1} + \mathbf{W}_{n,-1} - \mathbf{V}_{n,-1}\right], \tag{14}$$

$$\mathbf{e}_y e^{ikz} = (-i)\sum_n i^n \sqrt{\pi(2n+1)}\left[\mathbf{W}_{n,+1} + \mathbf{V}_{n,+1} - \mathbf{W}_{n,-1} + \mathbf{V}_{n,-1}\right]. \tag{15}$$

B. Boundary condition solutions

Iterative simulation of multiple scattering in a dispersion of spherical particles first requires scattering solutions for the individual spheres. For scattering from a single solid sphere in a solid matrix, there will be an incoming incident field, a refracted internal field, and an outgoing scattered field for each of the **U**, **V**, and **W** wave fields. Each of these wave field components will also have an associated amplitude coefficient. Fig. 1 shows the relationship between each of the field components and the coefficients.

Single-sphere scattering has been solved numerous times in the literature, but often not in the most general form. These solutions mostly model the incident fields as plane waves with only a longitudinal or shear component.[18-23] Although these conditions are often sufficient for dilute suspensions, the incident fields for each particle in the iterative multipole approach will not in general be plane waves, but a combination of the initial plane waves and the scattered waves from other particles. Also, the incident fields will be a combination of both longitudinal and shear waves. Single-sphere scattering solutions were therefore required for arbitrary incident fields comprised of both longitudinal and shear waves.

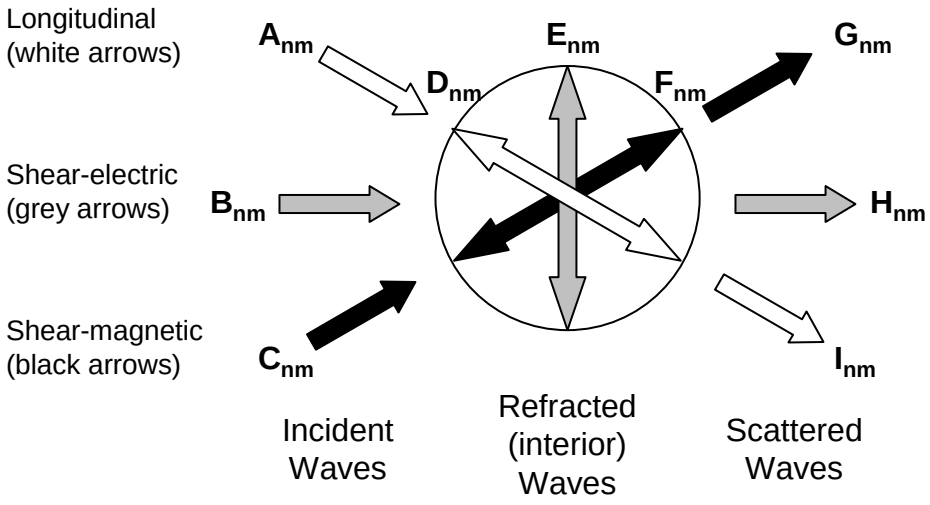

FIG. 1. Diagram of incident, refracted, and scattered elastic waves for single-particle scattering, with associated amplitude coefficients for the (*n*,*m*) multipole moment.

Given an arbitrary incident field, the amplitude coefficients of the refracted and scattered fields are found by solving the boundary conditions on the surface of the sphere. The boundary conditions provide a set of six linear equations for the six unknown coefficients. Three of these equations are obtained from continuity of the displacements, and the other three are derived from continuity of the stresses, where **u** is the vector displacement and σ is the stress tensor:

$$\mathbf{u}^{incident} + \mathbf{u}^{scattered} = \mathbf{u}^{refracted}, \tag{16}$$

$$\sigma^{incident} + \sigma^{scattered} = \sigma^{refracted}. \tag{17}$$

Orthogonality conditions for the vector spherical harmonics are used to eliminate the angular dependence from the boundary conditions. The resulting equations have the following matrix form which relate the six unknown coefficients to the three known coefficients:

$$\begin{pmatrix} \eta_1(j) & -\eta_1(h) & \eta_2(j) & -\eta_2(h) & 0 & 0 \\ \eta_6(j) & -\eta_6(h) & \eta_7(j) & -\eta_7(h) & 0 & 0 \\ \eta_4(j) & -\eta_4(h) & \eta_5(j) & -\eta_5(h) & 0 & 0 \\ \eta_9(j) & -\eta_9(h) & \eta_{10}(j) & -\eta_{10}(h) & 0 & 0 \\ 0 & 0 & 0 & 0 & \eta_3(j) & -\eta_3(h) \\ 0 & 0 & 0 & 0 & \eta_8(j) & -\eta_8(h) \end{pmatrix} \begin{pmatrix} D_{NM} \\ G_{NM} \\ E_{NM} \\ H_{NM} \\ F_{NM} \\ I_{NM} \end{pmatrix} = \begin{pmatrix} A_{NM}\eta_1(g) + B_{NM}\eta_2(g) \\ A_{NM}\eta_6(g) + B_{NM}\eta_7(g) \\ A_{NM}\eta_4(g) + B_{NM}\eta_5(g) \\ A_{NM}\eta_9(g) + B_{NM}\eta_{10}(g) \\ C_{NM}\eta_3(g) \\ C_{NM}\eta_8(g) \end{pmatrix}. \tag{18}$$

The η-symbols are functions of the spherical radial functions, multipole order *N*, longitudinal wave vector k_L, shear wave vector k_S, and the sphere radius *a*. The *j*, *h*, and *g* in the η-functions refer to the type of radial function used in η [$j = j_n(kr)$, $h = h_n^{(1)}(kr)$, and $g = h_n^{(2)}(kr)$]. The η-functions are given in the appendix, with the appropriate radial function substituting for *z*. Since the solution matrix separates into a 4×4 matrix and 2×2 matrix, the shear-magnetic fields are

decoupled from the longitudinal and shear-electric fields and do not participate in mode conversion. The scattering amplitudes for each sphere are obtained in the scattering model by solving the 2×2 and 4×4 matrices.

C. Translation of scattered fields

After computing the wave fields due to single-sphere scattering for all of the particles in the simulation, the scattered waves from each particle are then propagated to the other particles to become part of their incident wave fields. New scattered waves are then recomputed with use of the above boundary conditions, and the process is repeated. This procedure iteratively updates the incident fields with the multiple-scattering contributions until the amplitudes of the scattered waves converge. Since the scattered wave fields for each particle are in the original particle's coordinate system, the vector multipole functions for each particle must be transformed into the coordinate systems of the other particles in order to update the incident fields. This is accomplished with the use of special spherical wave expansions known as translational addition theorems. The transformation of the vector multipole functions from one coordinate system to another are expressed as follows:

$$\mathbf{U}_{nm} = \sum_{\nu=0}^{\infty} \sum_{\mu=-\nu}^{\nu} Q_{\nu\mu}^{nm} \mathbf{U}'_{\nu\mu} , \tag{19}$$

$$\mathbf{V}_{nm} = \sum_{\nu=0}^{\infty} \sum_{\mu=-\nu}^{\nu} \left(S_{\nu\mu}^{nm} \mathbf{V}'_{\nu\mu} + T_{\nu\mu}^{nm} \mathbf{W}'_{\nu\mu} \right), \tag{20}$$

$$\mathbf{W}_{nm} = \sum_{\nu=0}^{\infty} \sum_{\mu=-\nu}^{\nu} \left(S_{\nu\mu}^{nm} \mathbf{W}'_{\nu\mu} + T_{\nu\mu}^{nm} \mathbf{V}'_{\nu\mu} \right). \tag{21}$$

Fig. 2 shows the geometric relationship for the field translations between two spherical particles. The untranslated fields $\mathbf{U}_{nm}$, $\mathbf{V}_{nm}$, and $\mathbf{W}_{nm}$ in Eqs. (19)-(21) represent waves scattered from the original or "transmitting" sphere α, and are in sphere α's coordinate system. The translated fields $\mathbf{U}'_{\nu\mu}$, $\mathbf{V}'_{\nu\mu}$, and $\mathbf{W}'_{\nu\mu}$ represent the scattered waves incident on a second or "receiving" sphere β, and are transformed to sphere β's coordinate system. The global position vectors for the two spheres are $\mathbf{R}_\alpha$ and $\mathbf{R}_\beta$. The position of sphere α with respect to sphere β is therefore $\mathbf{R}_{\alpha\beta} = \mathbf{R}_\alpha - \mathbf{R}_\beta$. The translation vector $\mathbf{r}_\alpha$ is in sphere α's local coordinate system. The translational addition theorems therefore express the vector multipole functions in the α coordinate system (r_α, θ_α, and φ_α) as expansions of multipole functions in the β coordinate system (r_β, θ_β, and φ_β). These translation coefficients are only valid on the surface of sphere β ($r_\beta = a_\beta$, where a_β is the radius of sphere β). Note that the center of sphere α must lie outside of sphere β ($a_\beta < R_{\alpha\beta}$). This restricts the use of the addition theorems to spheres external to each other and non-overlapping. Although addition theorems can also be derived for spheres embedded within larger spheres ($a_\beta > R_{\alpha\beta}$), this work will only concern itself with the more commonly used external forms.

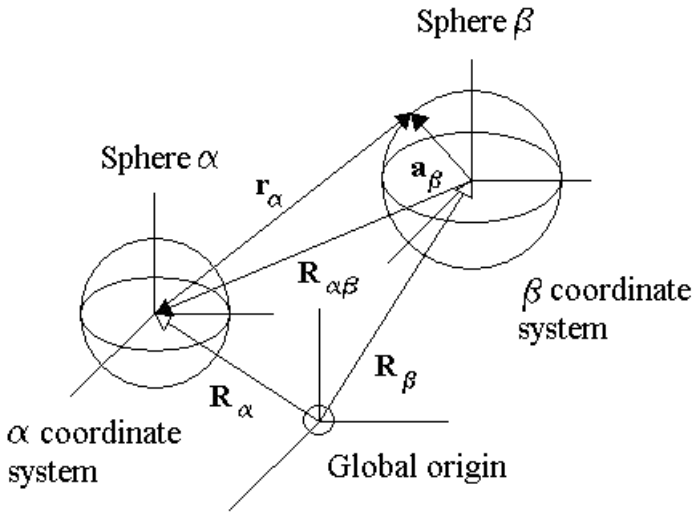

FIG. 2. Position ($\mathbf{R}_\alpha$ and $\mathbf{R}_\beta$) and translation ($\mathbf{r}_\alpha$) vectors for addition theorems with respect to local and global coordinates for spheres α and β.

The scalar addition theorem is sufficient for translating the longitudinal field since the longitudinal vector multipole function arises from a scalar potential [Eq. (7)]. The scalar addition theorem has been published extensively,[24-27] and provides the $Q_{\nu\mu}^{nm}$ translation coefficients:

$$Q_{\nu,\mu}^{n,m} = \sqrt{4\pi}\sum_{p=0}^{\infty}\left\{ i^{\nu-p-n} h_p^{(1)}(kR_{\alpha\beta}) Y_{p,m-\mu}(\Theta_{\alpha\beta},\Phi_{\alpha\beta}) \times C_{\nu,0,p,0}^{n,0} C_{\nu,\mu,p,m-\mu}^{n,m} \sqrt{\frac{(2\nu+1)(2p+1)}{(2n+1)}} \right\} . \quad (22)$$

The vector addition theorems are required to translate the shear fields since the transverse vector multipole functions arise from a vector potential. Cruzan was one of the earliest to derive expressions for the $S_{\nu\mu}^{nm}$ and $T_{\nu\mu}^{nm}$ translation coefficients by directly translating the coordinates in the vector spherical wave functions and applying various identities and relationships to arrive at an analytical solution.[28]

Another approach is to expand components of the vector multipole functions in the α coordinate system into expansions containing translation coefficients and vector spherical harmonics in the β coordinate system. The expression is then integrated in a manner similar to a Fourier series to determine the translation coefficients. The fields originating from sphere α are described by vector multipole functions containing terms of the form $h_l^{(1)}(kr_\alpha)\mathbf{Y}_{nm}^l(\theta_\alpha,\varphi_\alpha)$. Expanding these individual components in the β coordinate system yields the following:

$$h_l^{(1)}(kr_\alpha)\mathbf{Y}_{nm}^{l}(\theta_\alpha,\varphi_\alpha) = \sum_{\nu=0}^{\infty}\sum_{\lambda=\nu-1}^{\nu+1}\sum_{\mu=-\nu}^{+\nu}\left\{\Pi_{\lambda,\nu,\mu}^{l,n,m}(\mathbf{R}_{\alpha\beta})\mathbf{Y}_{\nu\mu}^{\lambda}(\theta_\beta,\varphi_\beta)\right\} \tag{23}$$

The expansion coefficients $\Pi_{\lambda,\nu,\mu}^{l,n,m}(\mathbf{R}_{\alpha\beta})$ are functions only of the relative position vector $\mathbf{R}_{\alpha\beta}$, and can be determined from the following integral:

$$\Pi_{\lambda,\nu,\mu}^{l,n,m}(\mathbf{R}_{\alpha\beta}) = \int_0^{2\pi} d\varphi_\beta \int_{-1}^{+1} d(\cos\theta_\beta) h_l^{(1)}(kr_\alpha) \times\left\{\mathbf{Y}_{nm}^{l}(\theta_\alpha,\varphi_\alpha)\cdot\mathbf{Y}_{\nu\mu}^{\lambda}{}^{*}(\theta_\beta,\varphi_\beta)\right\} \tag{24}$$

The values of the scattered α/incident β multipole fields are only relevant at the surface of sphere β, therefore $\Pi_{\lambda,\nu,\mu}^{l,n,m}(\mathbf{R}_{\alpha\beta})$ is integrated over the surface of sphere β with θ_β and φ_β as our variables of integration.

The integral is solved by first performing the dot product between the two vector spherical harmonics. The spherical harmonic terms in the α coordinate system are then expanded in terms of bipolar spherical harmonics containing products of spherical harmonics in the β (local) and αβ (global) coordinate systems.[13] The integration is then performed over the surface of sphere β, and the summation indices are simplified with the use of orthogonality conditions imposed by the Clebsch-Gordan coefficients. The final form for the expansion coefficients is the following:

$$\Pi_{\lambda,\nu,\mu}^{l,n,m}(\mathbf{R}_{\alpha\beta}) = j_\lambda(ka_\beta)\sum_{p=|l-\lambda|}^{l+\lambda}\left\{ i^{\lambda-l-p}h_p^{(1)}(kR_{\alpha\beta})Y_{p,m-\mu}(\Theta_{\alpha\beta},\Phi_{\alpha\beta}) \times C_{\lambda,0,p,0}^{l,0}\sqrt{\frac{4\pi(2\lambda+1)(2p+1)}{2l+1}} \times\sum_{\tau=-1}^{1}C_{l,m-\tau,1,\tau}^{n,m}C_{\lambda,\mu-\tau,1,\tau}^{\nu,\mu}C_{\lambda,\mu-\tau,p,m-\mu}^{l,m-\tau}\right\}. \tag{25}$$

Since the expansion coefficients in Eq. (25) only translate individual multipole terms in the **U**, **V**, and **W** wave functions, further derivation is required to transform the entire field expressions as given by Eqs. (20) and (21). To determine $S_{\nu\mu}^{nm}$ and $T_{\nu\mu}^{nm}$, it is first necessary to separate the spherical Bessel function from the expansion coefficients:

$$\Pi_{\lambda,\nu,\mu}^{l,n,m}(\mathbf{R}_{\alpha\beta}) = j_\lambda(ka_\beta)Z_{\lambda,\nu,\mu}^{l,n,m}(\mathbf{R}_{\alpha\beta}) \tag{26}$$

This provides vector multipole terms of the form $j_\lambda(ka_\beta)\mathbf{Y}_{\nu\mu}^{\lambda}(\theta_\beta,\varphi_\beta)$ for constructing fields incident to sphere β (note that the new incident fields are functions of spherical Bessel functions rather than spherical Hankel functions of the second kind):

$$h_l^{(1)}(kr_\alpha)\mathbf{Y}_{nm}^{l}(\theta_\alpha,\varphi_\alpha) = \sum_{\nu=0}^{\infty}\sum_{\lambda=\nu-1}^{\nu+1}\sum_{\mu=-\nu}^{+\nu} Z_{\lambda,\nu,\mu}^{l,n,m}(\mathbf{R}_{\alpha\beta})\, j_\lambda(ka_\beta)\mathbf{Y}_{\nu\mu}^{\lambda}(\theta_\beta,\varphi_\beta) \tag{27}$$

Two methods can then be used to derive expressions for $S_{\nu\mu}^{nm}$ and $T_{\nu\mu}^{nm}$. In the first method, the vector fields are translated directly using the expansion coefficients of Eq. (27) and equating the **U**, **V**, and **W** wave functions and associated scattered wave field coefficients with the **U**′, **V**′, and **W**′ wave functions and incident wave field coefficients. In the second method, the potentials for the fields are translated using Eq. (27). This method is possible since the fields can be derived from the vector potential $\mathbf{\Psi}$, and requires equating the potentials and corresponding amplitude coefficients and subsequently reconstructing the vector fields using Eqs. (8) and (9). Both methods produce a set of equivalent solutions for the translation coefficients $S_{\nu\mu}^{nm}$ and $T_{\nu\mu}^{nm}$, the simplest of which are the following:

$$S_{\nu\mu}^{nm} = Z_{\nu,\nu,\mu}^{n,n,m}, \tag{28}$$

$$\begin{aligned} T_{\nu\mu}^{nm} &= -i\sqrt{\frac{2\nu+1}{\nu+1}}Z_{\nu-1,\nu,\mu}^{n,n,m} = i\sqrt{\frac{2\nu+1}{\nu}}Z_{\nu+1,\nu,\mu}^{n,n,m} \\ &= i\sqrt{\frac{2n+1}{n+1}}Z_{\nu,\nu,\mu}^{n-1,n,m} = -i\sqrt{\frac{2n+1}{n}}Z_{\nu,\nu,\mu}^{n+1,n,m} \end{aligned}, \tag{29}$$

where

$$\begin{aligned} Z_{\lambda,\nu,\mu}^{l,n,m}(\mathbf{R}_{\alpha\beta}) = \sum_{p=|l-\lambda|}^{l+\lambda}\Bigg\{ & i^{\lambda-l-p}h_p^{(1)}(kR_{\alpha\beta})Y_{p,m-\mu}(\Theta_{\alpha\beta},\Phi_{\alpha\beta}) \\ & \times C_{\lambda,0,p,0}^{l,0}\sqrt{\frac{4\pi(2\lambda+1)(2p+1)}{2l+1}} \\ & \times \sum_{\tau=-1}^{1} C_{l,m-\tau,1,\tau}^{n,m} C_{\lambda,\mu-\tau,1,\tau}^{\nu,\mu} C_{\lambda,\mu-\tau,p,m-\mu}^{l,m-\tau}\Bigg\} \end{aligned}. \tag{30}$$

Testing of Eqs. (28-30) showed they are numerically equivalent to those of Cruzan.[20] Recurrence formulas have been derived for both the scalar and vector addition theorems, and significantly reduce the number of calculations for computing the translation coefficients.[21-23] However, the direct expressions in Eqs. (22) and (28-30) were used to demonstrate proof-of-concept for the modeling approach.

D. Multiple-scattering computations

The computations are performed by first calculating the scattered wave fields for each particle in the system due to an initial plane wave. The scattered wave fields are then translated

between all of the particles and summed for each particle. A new incident wave field (initial + scattered wave fields) is then used to compute revised scattered wave fields from each particle. This process is continued by iteration until the scattered wave fields converge (*i.e.*, no change in amplitude coefficients between consecutive iterations). Each iteration represents a successive order of scattering (first iteration = first-order multiple scattering, second iteration = second-order multiple scattering, *etc*.). Fig. 3 illustrates the computation process.

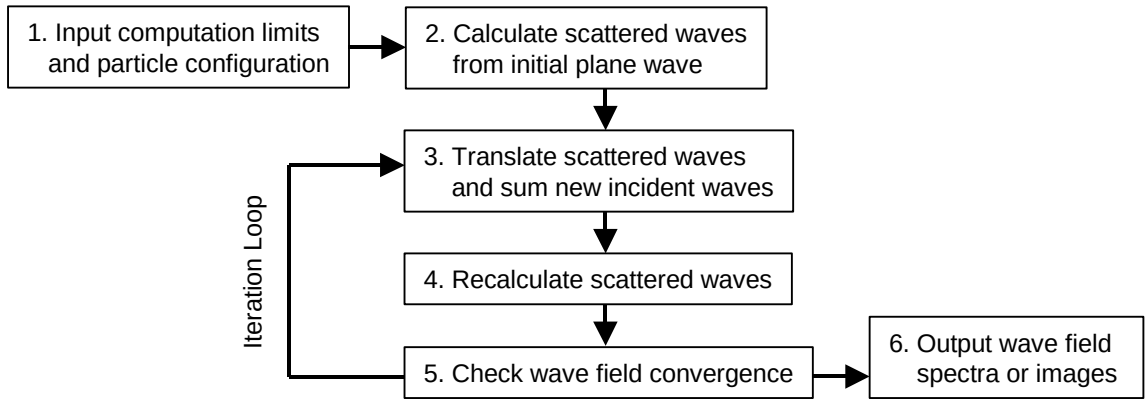

FIG. 3. Flow diagram of computation steps performed in the elastic wave scattering model.

The model can be configured to provide either wave field images or spectral results. Computation limits include the maximum multipole expansion order to compute (n_{max}), and the precision limit for stopping the iterations. Computer algorithms for the model were written, debugged, and compiled in Fortran 90. Simulations were performed on a personal desktop computer with 256 MB RAM and a 1.7 GHz processor to test the functioning and performance of the model. Computation times varied from a few minutes to 36 hours.

In addition to wave field images and attenuation spectra, it is also possible to model elastic wave velocity with the iterative multipole method. Although the vector multipole functions are time-independent solutions to the Navier equation, the ability to manipulate the amplitude of the initial plane wave as a function of frequency allows the simulation of pulses through the use of Fourier transforms. This is accomplished by modifying the spectral input for the initial plane wave with appropriate wavelet functions [Fig. 4(a)], calculating the interactions of the modified wave in the simulated particle pack, and applying an inverse Fourier transform to the resultant spectra. The inverse transform creates a wave pulse in the time domain. Analysis of the time delay between this pulse and one with the simulated particle pack absent, Fig. 4(b), provides the effective wave velocity (note that pulse attenuation can also be obtained). This procedure is equivalent to simulating the frequency characteristics of a transmitting ultrasonic transducer. The spatial characteristics of the transducer's wave field can also be modeled by appropriately modifying the multipole components of the initial wave. For example, a point source would produce wave fields comprised exclusively of monopole and dipole moments for the longitudinal and shear fields respectively.

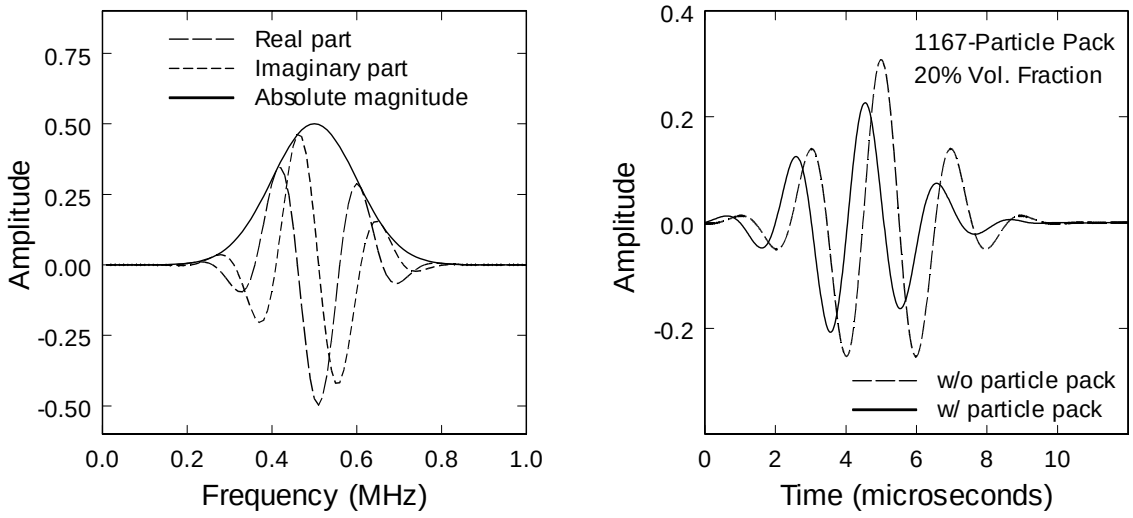

(a) (b)

FIG. 4. Modulation of the initial plane wave spectrum using wavelet transforms (a), and time-delay comparison of resultant pulses for an 1167-particle dispersion (b).

III. RESULTS

A. Simulations of two to sixteen particles

The scattering interactions between two particles were initially simulated to test the ability of the model to reproduce wave propagation phenomena. The particles were modeled as quartz spheres in a matrix of water ice, and the wave field patterns were imaged to reveal whether realistic wave behavior was simulated. The acoustic properties of quartz and ice are sufficiently different to clearly show scattering phenomena such as reflection, but not too different to preclude other types of wave propagation such as refraction through particles. Fig. 5 shows images of the scattered wave fields resulting from a longitudinal wave incident on two spheres aligned along the direction of wave propagation (from left to right in the images). The incident wave was not superimposed on the scattered wave fields in order to emphasize the scattering mechanisms, and the image grey scale is proportional to the scattered wave field amplitude. The images display both refractive focusing (forward scattering) of the longitudinal wave, Fig. 5(a), and mode conversion of a small part of the longitudinal wave to shear waves, Fig. 5(b).

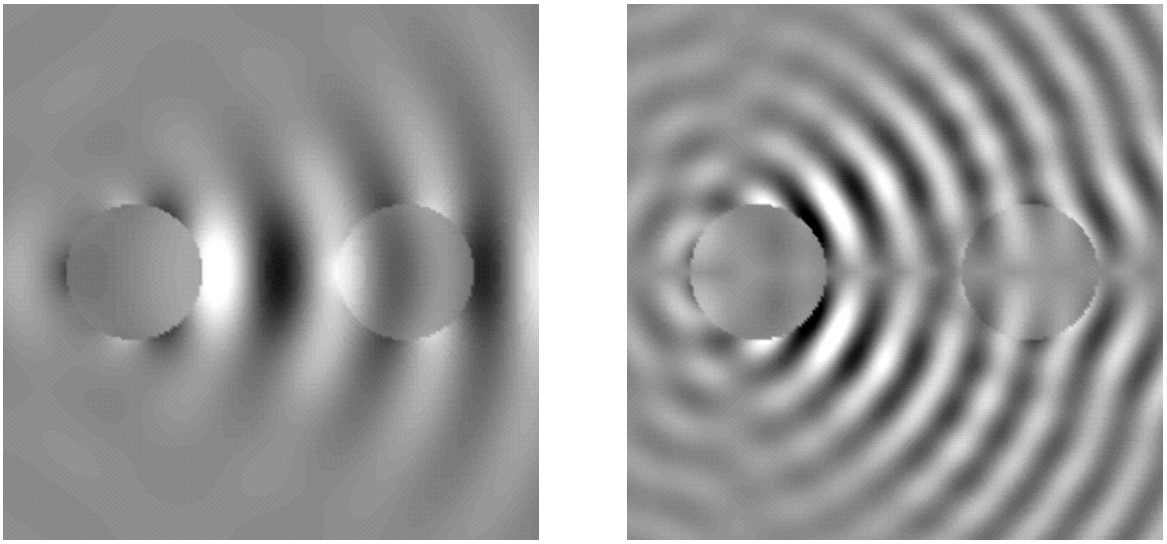

(a) (b)

FIG. 5. Wave field images of scattered waves resulting from an incident 5-MHz longitudinal wave with a pair of 1.0-mm diameter quartz spheres in ice: (a) Scattered longitudinal wave displaying focusing, and (b) scattered shear wave displaying mode conversion from longitudinal wave.

Since most of the wave behavior in Fig. 5 arises from single-sphere scattering, single-scattering computations were compared to the multiple-scattering computations to ascertain the differences between the two solutions and determine the effects of multiple scattering. The single-scattering computations superimpose the single-scattering solutions from each of the spheres to calculate the effective field. Figs. 6(a) and 6(b) are difference plots of the multiply scattered longitudinal and shear waves in Figs. 5(a) and 5(b), respectively, with the single-scattering solutions. The difference plots highlight the spatial regions where multiple scattering has the largest contribution to the wave fields. The images in Fig. 6 clearly show the primary effect of multiple scattering in the two-sphere configuration is the shielding of the second (right) sphere by the first (left) sphere.

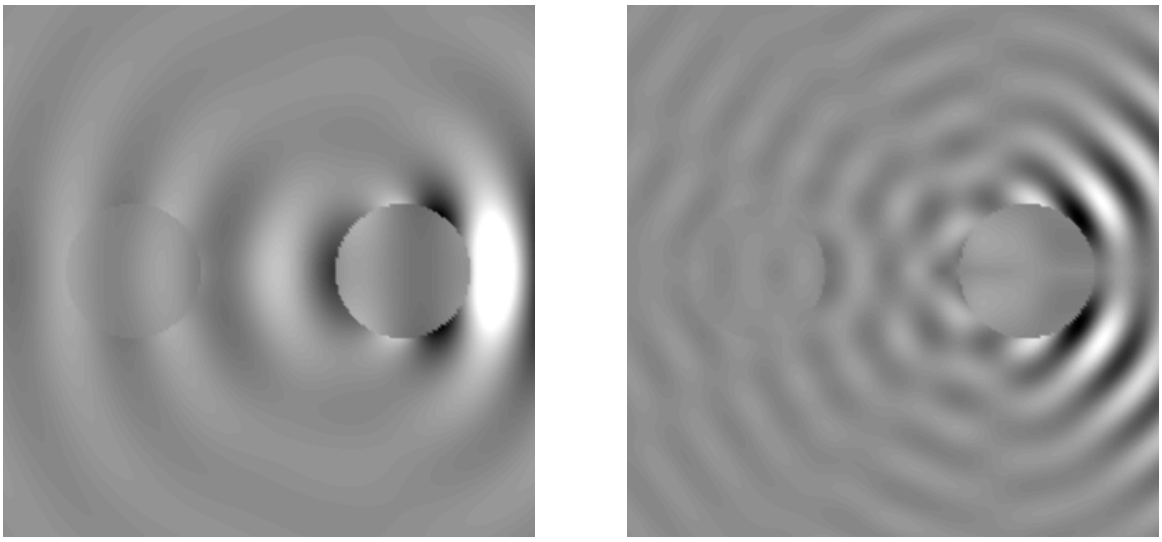

(a) (b)

FIG. 6. Displacement differences between multiple-scattering and single-scattering models for an incident longitudinal wave, showing a scattered longitudinal wave, *z* component (a), and a mode-converted shear wave, *x* component (b).

Simulations were subsequently performed for 2D dispersions containing up to 16 particles to gauge the model's ability to calculate multiple scattering in more complex structures. Fig. 7 displays the propagation of a plane wave with mixed longitudinal and shear components through an ordered [Fig. 7(a)] and random [Fig. 7(b)] configuration of quartz particles. Here the images show the *x* component of the shear fields, and the incident wave fields are superimposed on the scattered wave fields to give a truer representation of the elastic fields in the material system. Figure 7(a) shows the shear wave amplitude decreasing as it progresses from left to right through the particle lattice. A total decrease in peak-to-peak amplitude of 44% is observed across the image field. Since the constituent material properties are fully elastic with no built-in attenuation properties, the attenuation of the shear waves is due wholly to scattering. The attenuation probably arises from an acoustic band gap since the waves are passing though an ordered array with a lattice spacing commensurate with the wavelength. In contrast, Figure 7(b) shows localized wave field concentrations between and within certain particles. This localization of wave field energy may be due to resonance effects. Also, the wave front in Fig. 7(b) is distorted from the initial plane-wave geometry due to the disordered structure of the particles, in contrast to Fig. 7(a) where the planar wave front is preserved.

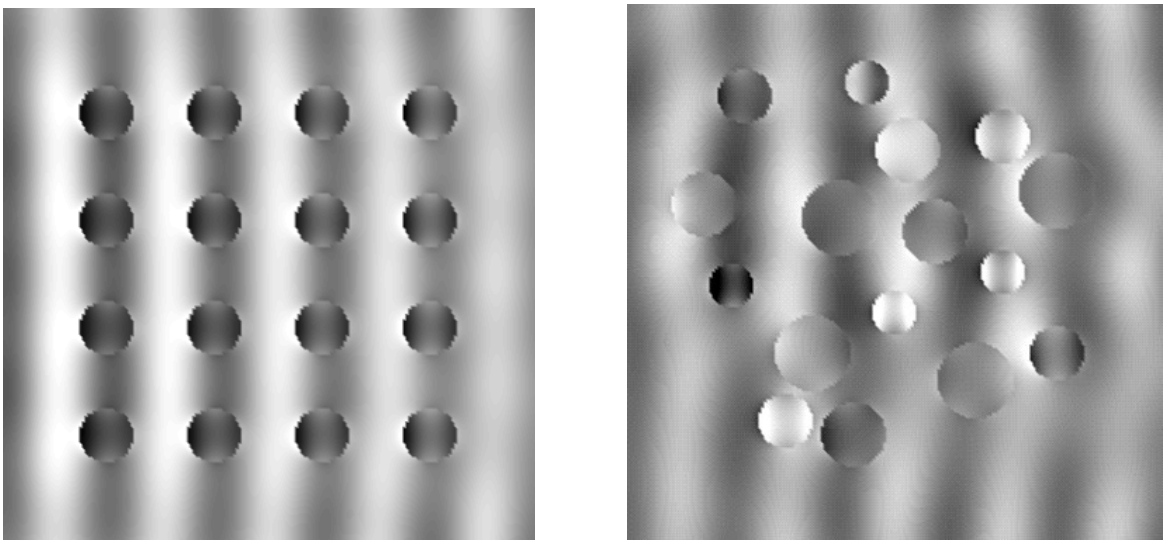

(a) (b)

FIG. 7. Total (scattered + incident) shear wave *x* component for an incident mixed longitudinal-shear wave at 1.0 MHz, for ordered (a) and disordered (b) configurations of quartz particles in ice (diameter = 0.8-1.4 mm).

The results from simulation of two to sixteen particles demonstrate the model's ability to reproduce basic wave propagation behavior such as refraction, mode conversion, and acoustic band gaps at a qualitative level. All of the above simulations were calculated to a maximum multipole order of $n_{max} = 6$.

B. Simulations of dispersions with 10^2-10^3 particles

Spectra and wave field images for larger 3D particle packs (100-700 particles) were also generated to demonstrate the ability to model actual material microstructures. Fig. 8 displays the simulated geometry [Fig. 8(a)] and spectra [Fig. 8(b)] for a cylindrical arrangement of 200-μm diameter NaCl particles in a soft polymer matrix. For the simulation of spectra, the wave fields are evaluated on a planar array of points with a circular shape. This array simulates the face of an ultrasonic transducer by averaging the wave field amplitudes over a defined area. This averaging is necessary since local interference effects arise when the fields are evaluated at a single point. The particle pack dimensions are also kept constant to eliminate effects due to changes in sample size. As shown in the spectra [Fig. 8(b)], the model predicts that the attenuation increases with particle volume fraction and frequency. These results are both intuitive (closer-packed particles lead to greater ultrasonic losses due to scattering) and supported by experiment.

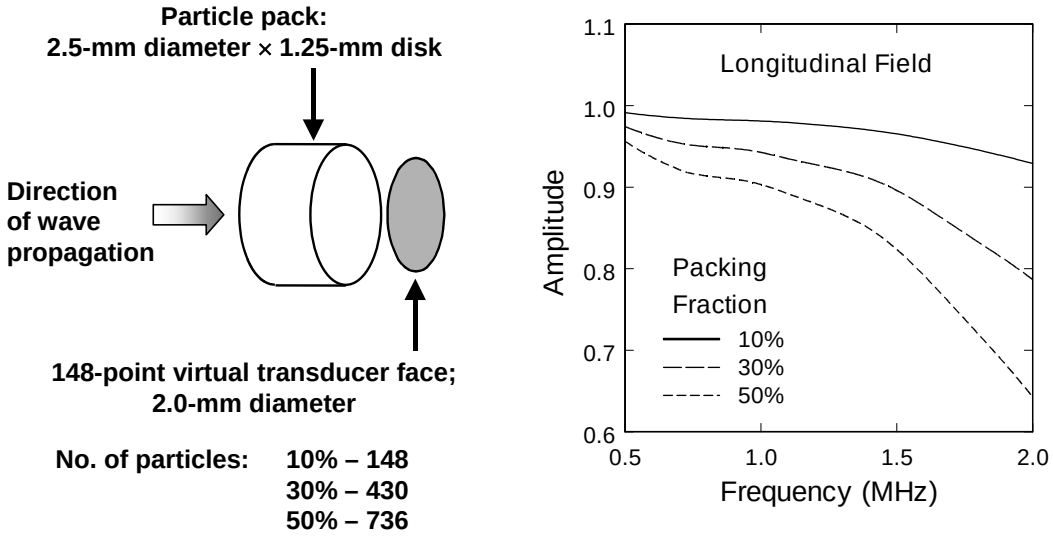

(a) (b)

FIG. 8. Simulation geometry (a) and spectra (b) for a random microstructure of 200-μm diameter NaCl particles in a soft polymer, displaying attenuation due to increased volume fraction of particles.

Fig. 9 compares the wave fields for periodic [Fig. 9(a)] and random [Fig. 9(b)] arrangements of 200-μm diameter particles in a soft polymer matrix at 50% volume fraction. The particle packings are three dimensional and cylindrical as shown in Fig. 8(a), with the image plane slicing through the center of the cylinder along the cylinder's axis. The incident wave is superimposed in these images in order to evaluate the effect of order/disorder on the total elastic wave field. The wave field images in Fig. 9 indicate greater fluctuation and non-uniformity for the elastic fields associated with the random particle configuration [Fig. 9(b)] as compared to the periodic lattice [Fig. 9(a)]. The ability to simulate both spectra and wave field patterns allows a more thorough characterization of wave propagation in a particle-filled medium. Both spectral [Fig. 8(b)] and wave field simulations [Fig. 9] were computed to a maximum multipole order of $n_{max} = 3$.

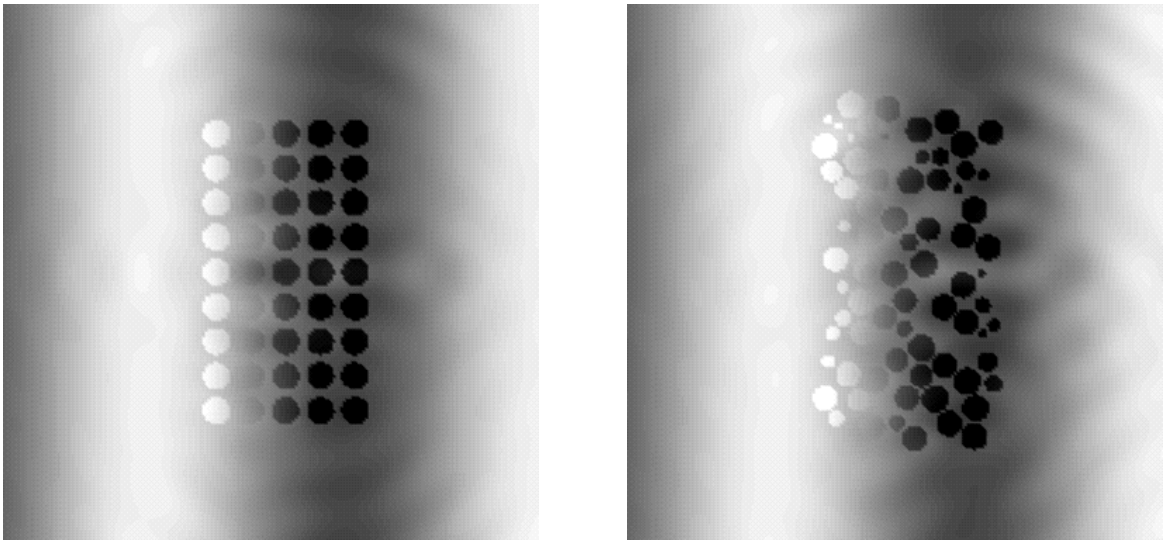

(a) (b)

FIG. 9. Wave field images of displacement resulting from an incident 0.5-MHz longitudinal wave in a cylindrical packing of 200-μm diameter NaCl particles in rubber at 50% volume fraction: (a) Body-centered-cubic (bcc) lattice of 649 particles, and (b) random packing of 736 particles.

The ability to predict elastic wave velocity was also demonstrated with simulations of dispersions containing 600-μm glass particles in a soft polymer matrix. The dispersions contained up to 3000 particles and 50% particle volume fraction. The results show an initial increase in effective velocity with increasing packing density up to 20%, which is consistent with experimental observations. However, above 20% particle volume the model under-predicts the velocity. These results demonstrate the viability of the Fourier transform method for modeling wave velocity in dispersions of spherical particles, but also indicate the current simulations are not accurate for dense packings. This deficiency can be attributed to a lack of convergence for the translational addition theorems at the n_{max} values used for the velocity simulations ($n_{max} = 4$). The next section examines the convergence properties of the model.

C. Convergence

The convergence properties of the model can be divided into three components: Convergence of the addition theorems, convergence of the spectra of the effective field, and convergence of the iterations. These components behave independent of one another; i.e., the convergence of one component is not dependent on the convergence of the other two. All three of these convergences, however, are dependent on the maximum computed multipole order (n_{max}), on the frequency of the propagating wave, and on the structure of the particle dispersion (particle distances, particle orientations, and degree of order-disorder). Convergence of all three components is necessary for computational fidelity.

Addition Theorem Convergence

The convergence of the addition theorems [Eqs. (19-21)] was numerically tested by translating the elastic fields from one sphere to an evaluation point on another sphere and comparing the translated fields to the untranslated fields at that point. Convergence was evaluated as a function of n_{max}, frequency, sphere size, sphere separation, orientation of the two spheres, and orientation of the evaluation point on the second sphere. Since the fields represented elastic fields in solids, the size and distance scale for the receiving sphere (sphere β) was in the centimeter range, and the frequencies were in the 0-1.0 MHz range.

All three multipole fields (**U**, **V**, and **W**) were tested with an initial quadrupole (n=2, m=1) moment. A quadrupole moment was chosen since most multiple-scattering methods seek to model many-body wave interactions beyond the dipole approximation, which becomes increasingly less accurate as scatterers become more closely spaced. Additionally, a quadrupole moment represents a good compromise between $n > 2$ moments and the simple dipole moments since computation time increases by approximately the sixth power of the multipole order. Also note the coupling between the **V** and **W** fields in the addition theorems [Eqs. (20-21)] requires the sum of the two transverse fields to be compared instead of the two fields individually (i.e., **V** + **W** is compared to **V'** + **W'**, rather than **V** to **V**' and **W** to **W**').

Following the coordinate conventions in Fig. 2, Figs. 10-13 are convergence plots for sphere β positioned at $\Theta_{\alpha\beta} = 34°$, $\Phi_{\alpha\beta} = 295°$, and with four separation distances ($R_{\alpha\beta}$ = 1.0, 2.0, 3.0, and 4.0 cm). The evaluation point on sphere β was positioned at $\theta_\beta = 163°$, $\varphi_\beta = 320°$, and a_β = 0.5 cm. Each figure displays results for a different frequency (0.01, 0.10, 0.50, and 1.00 MHz respectively). At low frequencies (Fig. 10), the results show that field translations converge more rapidly as a function of n_{max} for larger sphere separations. However, as the field frequency increases to 0.10 MHz, the convergence curves gradually shift and begin to overlap for the two most distant positions (Fig. 11). The curves continue to shift with higher frequency and overlap for all positions at 0.50 MHz (Fig. 12). The curves continue to shift, however, with increasing frequency and cross one another at 1.0 MHz (Fig. 13).

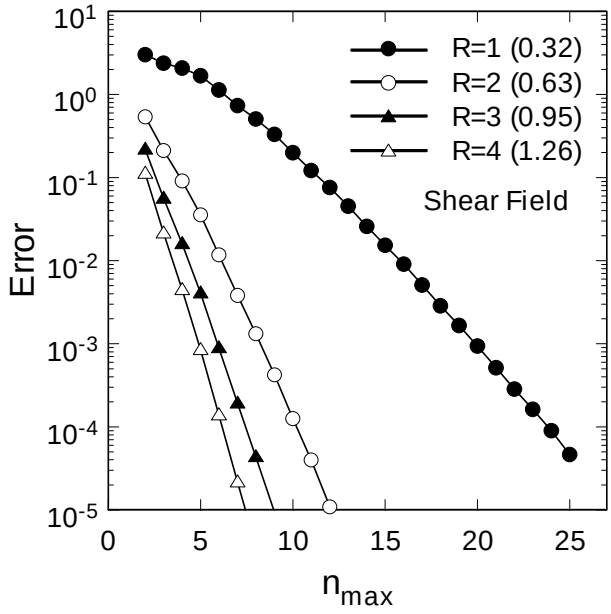

FIG. 10. Addition theorem convergence for translation of 0.01-MHz shear fields between two 1.0-cm diameter quartz spheres in ice. $R = R_{\alpha\beta}$ = center-to-center distance between spheres in cm. Numbers in parentheses are $kR_{\alpha\beta}$ values.

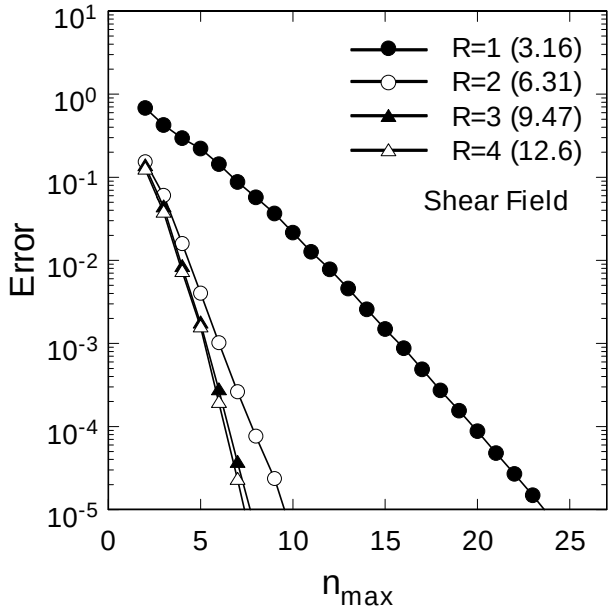

FIG. 11. Addition theorem convergence for translation of 0.10-MHz shear fields between two 1.0-cm diameter quartz spheres in ice. $R = R_{\alpha\beta}$ = center-to-center distance between spheres. Numbers in parentheses are $kR_{\alpha\beta}$ values.

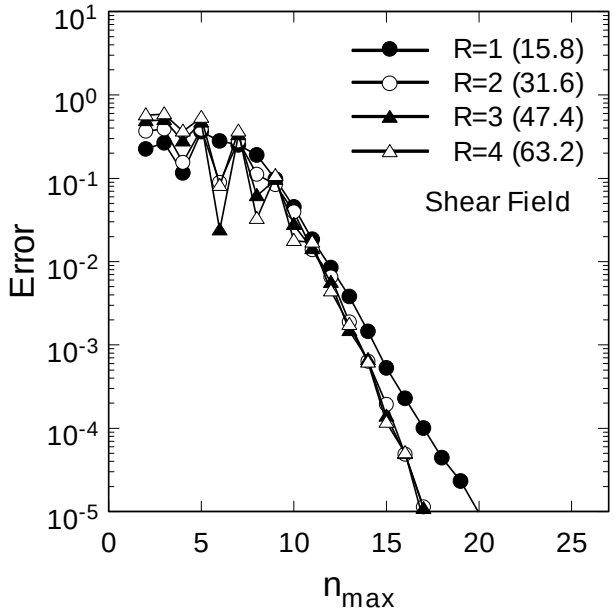

FIG. 12. Addition theorem convergence for translation of 0.50-MHz shear fields between two 1.0-cm diameter quartz spheres in ice. $R = R_{\alpha\beta}$ = center-to-center distance between spheres. Numbers in parentheses are $kR_{\alpha\beta}$ values.

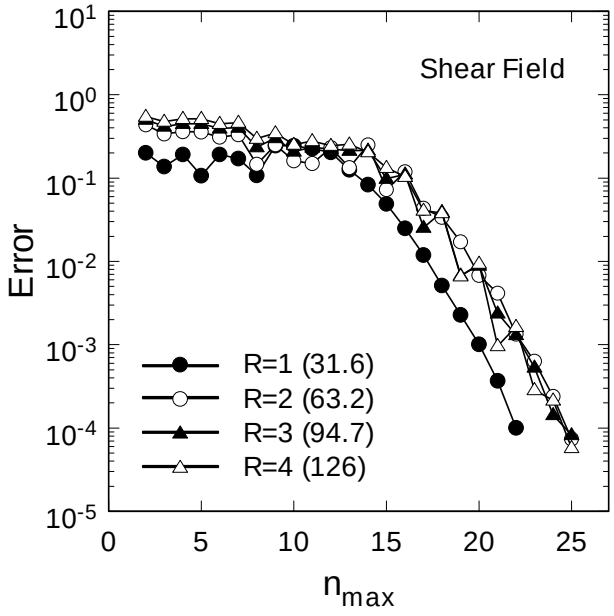

FIG. 13. Addition theorem convergence for translation of 1.00-MHz shear fields between two 1.0-cm diameter quartz spheres in ice. $R = R_{\alpha\beta}$ = center-to-center distance between spheres. Numbers in parentheses are $kR_{\alpha\beta}$ values.

The convergence curves indicate the degree of error present in the field translations for a specified n_{max}, frequency, and particle separation. For example, the convergence curves for Fig. 12 would correspond to the two-sphere simulations in Figs. 5 and 6 (since the frequency-sphere diameter parameter *kd* is equivalent). From Fig. 12, however, it is clear computations to $n_{max} = 6$ will result in field translation errors on the order of 10% for $R_{\alpha\beta} = 2$, and an n_{max} value of 12 is required to achieve errors on the order of 1%. Therefore, although the iteration sequence of the model may converge to a solution, the field translations, which are crucial to accurately representing the multiple-scattering interactions, may not be convergent and introduce various degrees of error into the solution.

Spectral Convergence

In multipole-based optical scattering models for single scatterers, the convergence of the scattered wave amplitudes as a function of frequency is dependent on the particle diameter *d* and maximum computed multipole order n_{max}. Simulation results verify the relationship between n_{max}, *d*, and convergence frequency ν_{max} (the highest frequency at which the wave fields converge) is proportional for multiple-scattering computations of elastic waves as well:

$$\nu_{\max} \approx \frac{3}{4\pi}\frac{c}{d} n_{\max}, \tag{31}$$

The symbol *c* is the wave velocity in the matrix. An example is the following. For longitudinal wave scattering from 1-mm diameter quartz particles in ice ($c_L = 3.98\times10^5$ cm/s) and for $n_{max} = 4$, the maximum frequency at which the spectrum converges is $\nu_{max} \approx 4$ MHz. This result indicates that the elastic wave spectra will be convergent for frequencies from 0-4 MHz at $n_{max} = 4$, but that higher n_{max} values will be required for convergence at higher frequencies. The spectral convergence is independent of addition theorem and iterative convergence, yet lack of spectral convergence can contribute significant error to multiple-scattering simulation results.

Iterative Convergence

Iterative convergence assures that the back-and-forth scattering interactions modeled with each iteration step converge to stable wave field amplitudes. This is physically required since each successive multiple scattering produces a diminishing contribution to the total field, eventually resulting in the final field configuration. Computationally, however, this convergence is not always assured due to numerical instabilities. Simulations of a variety of small and large particle packings have shown that all three elastic fields converge to within computational limits (10^{-16} for double precision) for random structures and a wide range of frequencies [Fig. 14(a)]. Both the longitudinal and shear-electric fields also converge for ordered structures such as cubic lattices [Fig. 14(b)]. However, the shear magnetic field does not converge at most frequencies for a cubic lattice, but rather displays fractional differences in amplitude on the order of 10^{-2} to 10^{-4} between iteration steps [Fig. 14(b)]. The origin of the nonconvergence for the shear-magnetic field has not yet been resolved. However, the nonconvergence has not affected most of the multiple-scattering simulations to date due to its small effect on the final field amplitudes and its limitation to ordered lattices. The failure of the shear-magnetic field to converge for ordered

lattices suggests the nonconvergence may be attributable to resonance effects, numerical instabilities, or both.

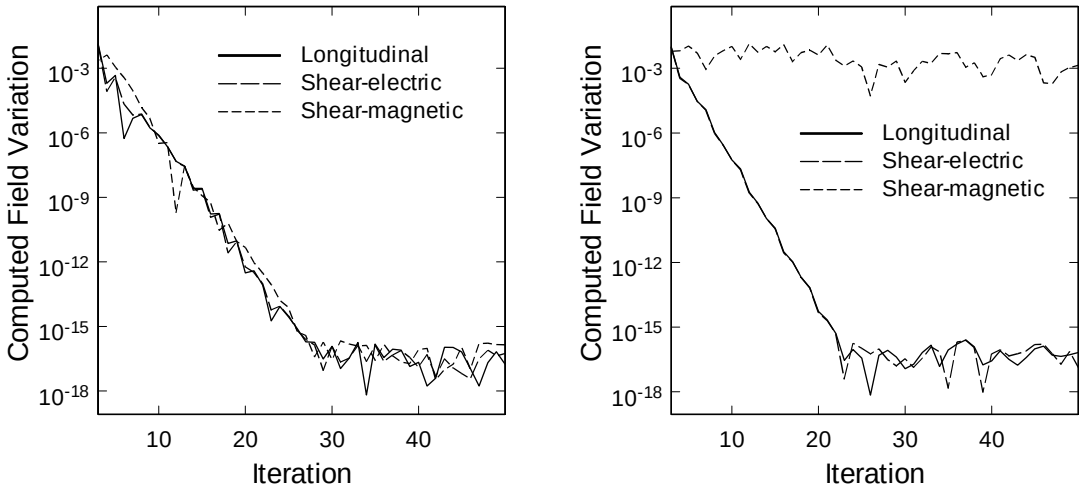

FIG. 14. Iterative convergence of simulations for a cluster of eight 1.0-mm diameter quartz particles in ice with incident 2.5-MHz longitudinal and shear waves: (a) Random cluster, and (b) cubic cluster.

In addition to dispersion structure (particle-particle orientations), iterative convergence has also been found to be dependent on frequency, average particle separation (volume fraction of particles), and n_{max}. Iterative convergence appears independent of both addition theorem and spectral convergence, however, indicating that all three convergence criteria must be considered in iterative multipole models.

IV. DISCUSSION

The results to date indicate the iterative multipole model reproduces realistic wave propagation behavior at a qualitative level. Phenomena such as mode conversion, refraction, scattering-induced attenuation, and band-gap attenuation have been observed in both wave field images and spectra. The model can also simulate large numbers of particles and complex random structures directly. Random particle packings of up to 3000 particles and 50% particle volume fraction have been modeled. The iterations are generally numerically stable and converge for most particle configurations and fields. The one exception that has been found is for the shear-magnetic field in cubic lattices, where the convergence of the iterations plateaus at an error of approximately 10^{-3}.

Addition theorem convergence is the current limiting factor for the iterative multipole approach implemented on a personal computer. Due to the intensive computations involved with the addition theorems, the maximum computed multipole order (n_{max}) has so far been limited to values of 3-6. Convergence studies of the addition theorems and model comparisons with experimental data indicate that these values are sufficient for dilute particle dispersions (up to

20% particle volume fraction), but are too low for denser packings. Consequently, simulations performed to date with high particle densities probably have significant error in the multiple-scattering contributions due to inadequate convergence of the field translations. The numerical stability of the iterative procedure is surprisingly robust, however, with iterative convergence unaffected by either addition theorem convergence or spectral convergence. Care must be taken, therefore, in interpreting the accuracy of the model results with regards to iterative convergence.

A common approach to validating numerical-based multiple-scattering models is to compare the results for a small cluster of spheres to other numerical approaches such as the boundary element method.[8] This approach is feasible for clusters of two or three spheres, but often becomes computationally intractable for large particle packings with more than a few dozen particles. Alternatively, model results can be compared to experimental data. This approach has been used extensively for evaluating classical formulations where multiple scattering is treated approximately.[32-33] Analogous experimental validation of the iterative multipole method is therefore an appropriate test for the model.

The current limitations of the iterative multipole model restrict its validity to dilute dispersions. Here the particles are spaced sufficiently to allow the use of low n_{max} values for addition theorem convergence. However, it is difficult to assess the accuracy of multiple-scattering computations for these conditions since single scattering dominates in dilute dispersions. One useful tool in evaluating the accuracy of the multiple-scattering computations is to compare their results to those of single-scattering computations for the same particle configuration. Such comparisons show that the iterative multipole model agrees with the single-scattering model for low n_{max} values. This is a consistent finding for low particle densities since the multiple-scattering contributions to the total elastic wave field will be small in comparison to the single-scattering contributions. It is also a consistent finding for high particle densities since it shows the low n_{max} values are insufficient for computing accurate translation coefficients for multiple scattering, again rendering their contribution to the total elastic wave field negligible.

The difficulty in validating the iterative multipole model with dilute particle packings extends to other multiple-scattering models as well, and additionally illustrates how single scattering can overwhelm contributions from multiple scattering. In such cases multiple-scattering models may produce accurate results for a particle dispersion, although the multiple scattering may be insufficiently or incorrectly calculated. Validation with dense particle systems is therefore necessary for accurately evaluating a model's performance.

The validation results to date for the iterative multipole model indicate that although the model appears to be running properly and accurately for dispersions with low particle densities, the computational limitation on n_{max} renders the model quantitatively inaccurate for dispersions with high particle densities. Fig. 15 illustrates this conclusion by comparing longitudinal wave velocity results for the iterative multipole model, the single-scattering model, and experimental measurements for 600-μm glass beads in an elastic polymer matrix. Note the agreement between the iterative multipole model and single-scattering model at high particle densities, indicating the insufficient computation of multiple scattering due to low n_{max}.

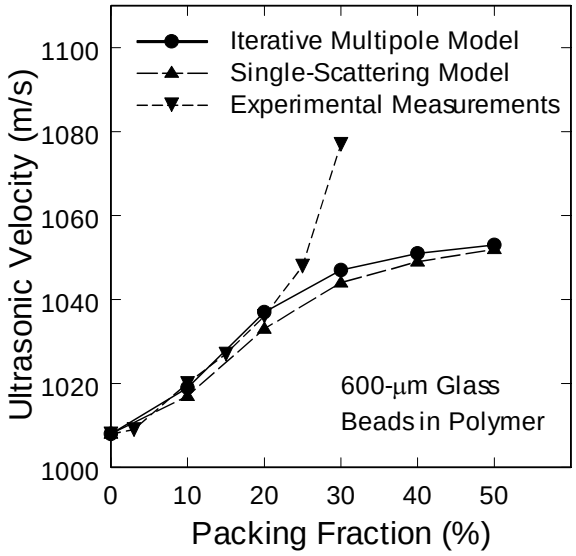

FIG. 15. Comparison of longitudinal wave velocity at 0.5 MHz for the iterative multipole model, the single-scattering model, and experimental measurements for 600-μm glass beads in an elastic polymer matrix.

Several solutions are available to resolve the computational limits to the iterative multipole method. These include increasing the speed and efficiency of the addition theorem computations with the use of recurrence algorithms.[29-31] The computations can also be simplified for fluid and mechanically soft matrices by limiting the propagating elastic fields to longitudinal waves. Finally, particle-particle interactions that do not significantly contribute to the multiple-scattering process (for example, from widely separated particles) can be omitted, thereby reducing the number of field translation computations. Other foreseeable improvements for the iterative multipole approach consist of expanding the ability to model more complex particulate systems. These include simulating viscoelastic media with the use of complex material properties and wave vectors, and simulating mixtures of spherical voids and particles.

In comparison to other multipole approaches, the iterative or order-of-scattering method appears to be a more direct and accessible approach for modeling elastic waves scattering in arbitrary dispersions of spherical particles. The iterative multipole method is numerically stable, particularly for random particle configurations, whereas stability cannot be guaranteed for inversion of large matrices. Finally, the iterative multipole method is a highly generalized approach that can be applied to dispersions of spherical scatterers of almost any configuration and composition. No fundamental assumptions or approximations about the dispersion structure are made. For example, the dispersion structure is not assumed to be random or homogeneous at large scale sizes as required by fast multipole methods. Additionally, the structure does not have to be built of repeating units or limited to two dimensions as is often the practice for finite methods.

V. CONCLUSIONS

An iterative multipole method has been developed to model arbitrary configurations of spherical, elastic particles in an elastic matrix, and has been implemented on a personal computer to test its functioning and performance. Initial results for systems of two to several hundred particles show that the model predicts many aspects of elastic wave behavior at the qualitative level. The model is also quantitatively accurate for dispersions with low particle densities (<20% particle volume fraction). However, assessing the accuracy of a multiple-scattering model for dilute dispersions is difficult since single-scattering interactions dominate. At higher particle densities, the model predictions deviate due to limitations in computing sufficiently high multipole orders (n_{max} = 8-16) for convergence of the addition theorems. Methods for resolving these limitations include the use of recurrence formulas for computing the addition theorems, approximations that reduce the number of computations by limiting the multiple scattering to the most significant interactions, and implementation of the model on larger computer systems.

ACKNOWLEDGMENTS

This work was supported by ATK-Thiokol, Inc. and the Air Force Research Laboratory under contract number F04611-98-C-0005. The author thanks I. Lee Davis, Lee H. Pearson, J. R. Dennison, Gregory A. Ruderman, and Brent L. Carruth for their technical assistance.

APPENDIX

The η functions for solution of the elastic wave boundary condition matrix, Eq. (18) are presented below. The η's are functions of the multipole order N, longitudinal wave vector k_L, shear wave vector k_S, and the sphere radius a. The spherical radial functions are denoted by z, and vary according to the radial function designated in Eq. (18) [$j = j_n(kr)$, $h = h_n^{(1)}(kr)$, and $g = h_n^{(2)}(kr)$].

$$\eta_1(z) = N\frac{z_N(k_L a)}{k_L a} - z_{N+1}(k_L a), \tag{A1}$$

$$\eta_2(z) = i\sqrt{(N)(N+1)}\,\frac{z_N(k_S a)}{k_S a}, \tag{A2}$$

$$\eta_3(z) = z_N(k_S a), \tag{A3}$$

$$\eta_4(z) = \frac{z_N(k_L a)}{k_L a}, \tag{A4}$$

$$\eta_5(z) = \frac{i}{\sqrt{(N)(N+1)}} \times \left[(N+1)\frac{z_N(k_S a)}{k_S a} - z_{N+1}(k_S a) \right], \tag{A5}$$

$$\eta_6(z) = -\lambda k_L z_N(k_L a) + 2\mu k_L \left\{ \left[\frac{(N-1)(N)}{(k_L a)^2} - \frac{N+1}{N+2} \right] z_N(k_L a) + \frac{z_{N+1}(k_L a)}{k_L a} \right\}, \tag{A6}$$

$$\eta_7(z) = 2i\mu k_S \sqrt{(N)(N+1)} \times \left[(N-1)\frac{z_N(k_S a)}{(k_S a)^2} - \frac{z_{N+1}(k_S a)}{k_S a} \right], \tag{A7}$$

$$\eta_8(z) = \mu k_S \left[(N-1)\frac{z_N(k_S a)}{k_S a} - z_{N+1}(k_S a) \right], \tag{A8}$$

$$\eta_9(z) = 2\mu k_L \left[(N-1)\frac{z_N(k_L a)}{(k_L a)^2} - \frac{z_{N+1}(k_L a)}{k_L a} \right], \tag{A9}$$

$$\eta_{10}(z) = \frac{i\mu k_S}{\sqrt{(N)(N+1)}} \times \left[\left[\frac{2(N^2-1)}{(k_S a)^2} - \frac{N+1}{N+2} \right] z_N(k_S a) + \frac{z_{N+1}(k_S a)}{k_S a} \right]. \tag{A10}$$

REFERENCES

1. R. Marklein, K. J. Langenberg, R. Bärmann, K. Mayer, and S. Klaholz, "Nondestructive Testing with Ultrasound: Numerical Modeling and Imaging," in *Acoustical Imaging, Vol. 22*, edited by P. Tortoli and L. Masotti (Plenum Press, New York, 1996), pp. 757-764.

2. A. A. Gusev, "Numerical identification of the potential of whisker and platelet filled polymers," Macromolecules **34**, 3081-3093 (2001).

3. V. E. Ostashev, D. K. Wilson, L. Liu, D. F. Aldridge, N. P. Symons, and D. Marlin, "Equations for finite-difference, time domain simulation of sound propagation in moving inhomogeneous media and numerical implementation," J. Acoust. Soc. Am. **117**, 503-517 (2005).

4. A-K. Hamid, I. R. Ciric, and M. Hamid, “Iterative solution of the scattering by an arbitrary configuration of conducting or dielectric spheres,” IEE Proceedings-H **138**, 565-572 (1991).

5. K. A. Fuller and G. W. Kattawar, “Consummate solution to the problem of classical electromagnetic scattering by an ensemble of spheres. II. Clusters of arbitrary configuration,” Opt. Lett. **13**, 1063-1065 (1988).

6. D. W. Mackowski, “Analysis of radiative scattering for multiple sphere configurations,” Proc. R. Soc. Lond. A **433**, 599-614 (1991).

7. S. Koc and W. C. Chew, “Calculation of acoustical scattering from a cluster of scatterers,” J. Acoust. Soc. Am. **103**, 721-734 (1998).

8. N. A. Gumerov and R. Duraiswami, “Computation of scattering from N spheres using multipole reexpansion,” J. Acoust. Soc. Am. **112**, 2688-2701 (2002).

9. Z. Liu, C. T. Chan, P. Sheng, A. L. Goertzen, and J. H. Page, “Elastic wave scattering by periodic structures of spherical objects: Theory and experiment,” Phys. Rev. B **62**, 2446-2457 (2000).

10. L. Greengard and V. Rokhlin, “A fast algorithm for particle simulations,” J. Comput. Phys. **73**, 325-348 (1987).

11. W. Greiner and J. A. Maruhn, *Nuclear Models* (Springer-Verlag, Berlin, 1996).

12. K. S. Thorne, “Multipole expansions of gravitational radiation,” Rev. Mod. Phys. **52**, 299-339 (1980).

13. D. A. Varshalovich, A. N. Moskalev, and V. K. Khersonskii, *Quantum Theory of Angular Momentum*, (World Scientific, Singapore, 1988).

14. J. A. Stratton, *Electromagnetic Theory* (McGraw-Hill, New York, 1941).

15. M. E. Rose, *Elementary Theory of Angular Momentum* (John Wiley and Sons, New York, 1957).

16. A. R. Edmonds, *Angular Momentum in Quantum Mechanics* (Princeton University Press, Princeton, New Jersey, 1957).

17. J. D. Jackson, *Classical Electrodynamics*, second edition (John Wiley and Sons, New York, 1975).

18. C. F. Ying and R. Truell, “Scattering of a plane longitudinal wave by a spherical obstacle in an isotropically elastic solid,” J. Appl. Phys. **27**, 1086-1097 (1956).

19. L. Knopoff, “Scattering of shear waves by spherical obstacles,” Geophysics **24**, 209-219 (1959).

20. L. Knopoff, “Scattering of compression waves by spherical obstacles,” Geophysics, **24**, 30-39 (1959).

21. N. G. Einspruch, E. J. Witterholt, and R. Truell, “Scattering of a plane transverse wave by a spherical obstacle in an elastic medium,” J. Appl. Phys. **31**, 806-818 (1960).

22. D. L. Jain and R. P. Kanwal, “Scattering of P and S waves by spherical inclusions and cavities,” J. Sound Vib. **57**, 171-202 (1978).

23. M. K. Hinders, “Plane-elastic-wave scattering from an elastic sphere,” Nuovo Cimento B **106B**, 799-817 (1991).

24. B. Friedman and J. Russek, “Addition theorems for spherical waves,” Q. Appl. Math. **12**, 13-23 (1954).

25. M. E. Rose, “The electrostatic interaction of two arbitrary charge distributions,” J. Math. Phys. (Cambridge, Mass.) **37**, 215-222 (1958).

26. S. Stein, “Addition theorems for spherical wave functions,” Q. Appl. Math. **19**, 15-24 (1961).

27. R. A. Sack, “Three-dimensional addition theorem for arbitrary functions involving expansions in spherical harmonics,” J. Math. Phys. (N.Y.) **5**, 252-259 (1964).

28. O. R. Cruzan, “Translational addition theorems for spherical vector wave functions,” Q. Appl. Math. **20**, 33-40 (1962).

29. W. C. Chew, “Recurrence relations for three-dimensional scalar vector addition theorem,” J. Electromagn. Waves Appl. **6**, 133-142 (1992).

30. W. C. Chew and Y. M. Wang, “Efficient ways to compute the vector addition theorem,” J. Electromagn. Waves Appl. **7**, 651-665 (1993).

31. D. W. Mackowski, “Calculation of total cross sections of multiple-sphere clusters,” J. Opt. Soc. Am. A **11**, 2851-2861 (1994).

32. L. W. Anson and R. C. Chivers, “Ultrasonic velocity in suspensions of solids in solids—a comparison of theory and experiment,” J. Phys. D: Appl. Phys. **26**, 1506-1575 (1993).

33. R. E. Challis, J. S. Tebbutt, and A. K. Holmes, “Equivalence between three scattering formulations for ultrasonic wave propagation in particulate mixtures,” J. Phys. D: Appl. Phys. **31**, 3481-3497 (1998)